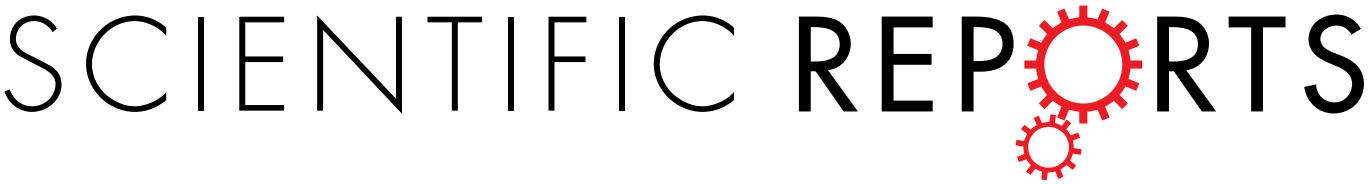

OPEN

Received: 05 August 2016
Accepted: 05 January 2017
Published: 13 February 2017

Crystalline Structure, Defect Chemistry and Room Temperature Colossal Permittivity of Nd-doped Barium Titanate

Qiaomei Sun[1,2], Qilin Gu[1,2], Kongjun Zhu[1], Rongying Jin[3], Jinsong Liu[2], Jing Wang[1] & Jinhao Qiu[1]

Dielectric materials with high permittivity are strongly demanded for various technological applications. While polarization inherently exists in ferroelectric barium titanate ($BaTiO_3$), its high permittivity can only be achieved by chemical and/or structural modification. Here, we report the room-temperature colossal permittivity (~760,000) obtained in *x*Nd: $BaTiO_3$ ($x = 0.5$ mol%) ceramics derived from the counterpart nanoparticles followed by conventional pressureless sintering process. Through the systematic analysis of chemical composition, crystalline structure and defect chemistry, the substitution mechanism involving the occupation of Nd^{3+} in Ba^{2+} -site associated with the generation of Ba vacancies and oxygen vacancies for charge compensation has been firstly demonstrated. The present study serves as a precedent and fundamental step toward further improvement of the permittivity of $BaTiO_3$-based ceramics.

The development of high-energy-density storage devices is extremely urgent for the sake of advanced microelectronics and communications[1–3]. Of great importance is to search for appropriate dielectric materials with high permittivity[4,5]. Inorganic ceramic materials with high dielectric constant have received extensive attention, due to their application in multilayer ceramic capacitors (MLCC)[6] and inorganic-organic hybrid flexible composite films[7]. The dielectric properties of inorganic ceramic materials can be improved *via* chemical modification[8,9] and/or grain-size engineering[10]. Among them, rare-earth element(s) doped $BaTiO_3$ (RE: $BaTiO_3$) has been considered as one of the most suitable materials for ferroelectric capacitors, because of its colossal dielectric constant (CDC)[11]. The incorporation of trivalent RE ions (such as La^{3+} and Nd^{3+}) can effectively enhance the room temperature permittivity of $BaTiO_3$[12,13], thereby improving the performance of relevant energy storage devices. In addition, the dielectric properties of $BaTiO_3$ can be tuned by varying the grain size; that is, with the decreasing grain size, the permittivity initially increases and then decreases after reaching a maximum at a critical grain size[10].

The permittivity of RE: $BaTiO_3$ is intimately related to the structural distortion and chemical defects surrounding the dopants. Theoretical calculations in terms of tolerance factor have indicated that the occupation of the exotic ions depends on their radius[14,15]. Since the radius of RE ions is usually between Ba^{2+}(1.35 Å) and Ti^{4+}(0.68 Å), larger RE^{3+} ions such as La^{3+} (1.15 Å) and Nd^{3+}(1.08 Å) prefer to substitute for the Ba^{2+} -site (A-site), and the smaller ones such as Yb^{3+}(0.87 Å) may locate exclusively at the Ti^{4+} -site (B-site), while the intermediate ones such as Y^{3+}(0.93 Å) and Er^{3+}(0.96 Å) may occupy both the A- and B- sites[16,17]. Accompanying with the specific doping, chemical inhomogeneity is often introduced. For example, the partial replacement of the A-site by La^{3+}would give rise to either the formation of Ti vacancies or the reduction of Ti[18]. These defects could significantly affect the dielectric properties of $BaTiO_3$-based ceramics. As demonstrated by Guillemet-Fritsch *et al.*[19], a room-temperature colossal permittivity (ε_{eff} ~800,000) was obtained in $Ba_{0.95}La_{0.05}TiO_{3-x}$ ceramics sintered by the spark plasma sintering (SPS) method, in which Ti^{3+}/Ti^{4+} acted as polaron carriers.

[1]State Key Laboratory of Mechanics and Control of Mechanical Structures, College of Aerospace Engineering, Nanjing University of Aeronautics and Astronautics, Nanjing 210016, China. [2]College of Materials Science and Technology, Nanjing University of Aeronautics and Astronautics, Nanjing 210016, China. [3]Department of Physics and Astronomy, Louisiana State University, Baton Rouge, LA 70803, USA. Correspondence and requests for materials should be addressed to K.Z. (email: kjzhu@nuaa.edu.cn)

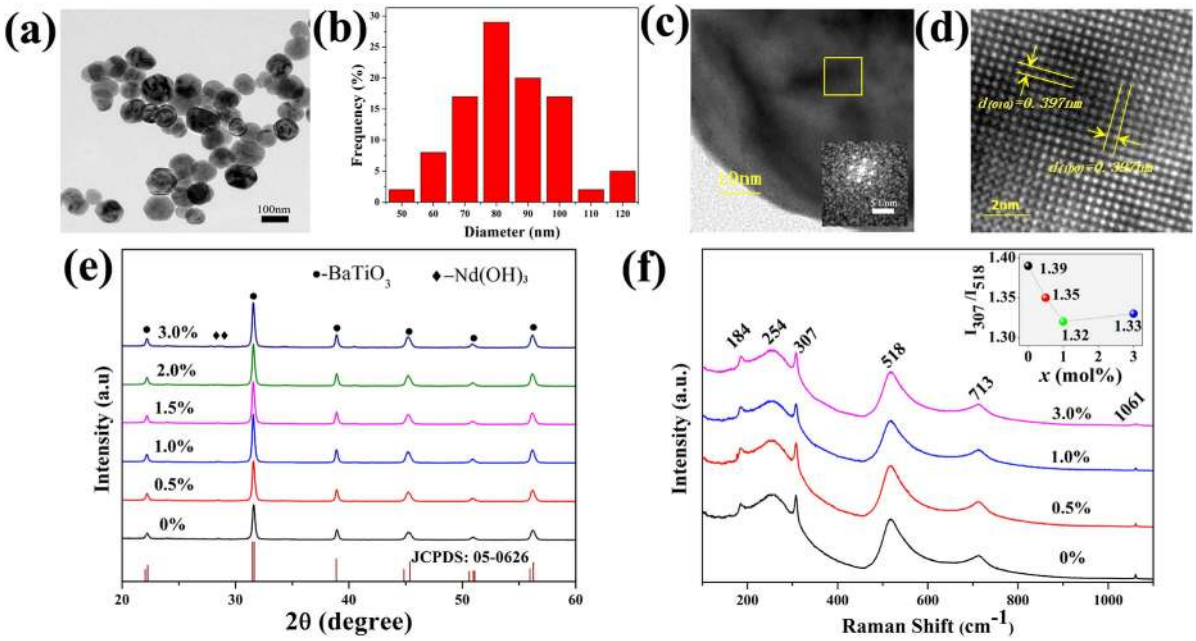

Figure 1. (**a**) TEM image of pure $BaTiO_3$ nanoparticles; (**b**) Particle size distribution of pure $BaTiO_3$ nanoparticles; (**c**) TEM image of an individual particle and its fast Fourier transform pattern in the inset; (**d**) HR-TEM image of the selected area marked by the yellow square in (**c**); (**e**) XRD patterns of *x*Nd: $BaTiO_3$ nanoparticles with indication of nominal Nd concentration; (**f**) Raman spectra of *x*Nd: $BaTiO_3$ samples with the inset showing the Nd-doping dependence of the relative intensity of peaks at 307 and 518 cm^{-1}.

Although Nd: $BaTiO_3$ ceramics have been studied[13,20–22], the mechanism for their improved permittivity (~300,000) remains unclear[13]. In addition, Nd: $BaTiO_3$ powders in the previous reports are often prepared by solid-state reaction (SSR), and high-temperature treatment (above 800 °C) is usually required, which results in large grain size and poor sintering activity. To achieve high bulk density and improved dispersion in organic matrix, ultrafine Nd: $BaTiO_3$ nanoparticles with pure phase and uniform particle size are highly desirable yet challenging. Although it is well known that hydrothermal synthesis can yield high-purity nanoparticles with narrow size distribution[23,24], the synthesis of RE: $BaTiO_3$ nanoparticles has been rarely reported[25,26]. Recently, we have synthesized monodispersed $BaTiO_3$ nanoparticles *via* the sol-hydrothermal method[27]. In this work, *x*Nd: $BaTiO_3$ ($x = 0$ ~3 mol%) nanocrystals were prepared by a similar process and their crystalline structure and defect chemistry were investigated elaborately. Subsequently, *x*Nd: $BaTiO_3$ ceramics were fabricated by a conventional pressureless sintering method. It's found that the dielectric constant was dramatically modified upon Nd doping. Especially, the colossal dielectric constant was observed in the sample with 0.5 mol% Nd at room temperature, and possible mechanisms for such effect were provided.

Results and Discussion

Crystalline structure analysis of *x*Nd: $BaTiO_3$ nanocrystals. The as-prepared *x*Nd: $BaTiO_3$ nanocrystals were characterized by various techniques. Figure 1a shows the transmission electron microscopy (TEM) image of pure $BaTiO_3$. The size distribution of these spherical particles is displayed in Fig. 1b, indicating that the diameter of majority particles (~90%) is in the range of 60~100 nm. Zooming into an individual nanoparticle (Fig. 1c), a single crystal character is revealed, as demonstrated by the fast Fourier transform (FFT) pattern (the inset of Fig. 1c) and well-defined atomic arrangement in the HR-TEM image in Fig. 1d. The interplanar spacing of the lattice is 0.397 nm, corresponding to (100) plane in tetragonal $BaTiO_3$.

The tetragonal structure of nanoparticles has been further confirmed by X-ray diffraction (XRD) patterns. As shown in Fig. 1e, all XRD peaks obtained from pure $BaTiO_3$ nanoparticles are well-matched with the tetragonal structure corresponding to Joint Committee on Powder Diffraction Standards (JCPDS) Files No. 05-0626. These peaks remain in the *x*Nd: $BaTiO_3$ nanocrystals (see Fig. 1e). Inductively coupled plasma optical emission spectrometry (ICP-OES) was further carried out to quantify the chemical composition of samples. As listed in Table 1, the actual Nd concentration is found to be 0, 0.49, 0.95 and 1.43 mol% for nominal *x*Nd: $BaTiO_3$ samples with $x = 0$, 0.5, 1.0 and 1.5 mol%, respectively. The result indicates that the Nd ions have almost completely incorporated into the $BaTiO_3$ structure.

However, additional peaks (as indicated by diamond symbol) appear in the sample with $x = 2$ mol%, which can be assigned to $Nd(OH)_3$ impurity phase (JCPDS No. 06-0601). Also, the energy dispersive X-ray spectroscopy (EDX) analysis results in Supplementary Fig. S2 confirm that rod-like impurity can be attributed to $Nd(OH)_3$.

To confirm that the $BaTiO_3$ nanocrystals form only tetragonal structure at room temperature, we further measured Raman vibrational spectroscopy, as it is sensitive to the structure symmetry[1,28]. As can be seen from Fig. 1f, all Raman scattering spectra consist of bands around 184, 254, 307, 518 and 713 cm^{-1}, which are the

Nominal composition	Analyzed composition	
	Ba/Ti	Nd (*x* mol)
$BaTiO_3$	1.015	0%
0.5%Nd: $BaTiO_3$	0.994	0.49%
1.0% Nd: $BaTiO_3$	1.002	0.95%
1.5% Nd: $BaTiO_3$	0.991	1.43%

Table 1. Nominal versus ICP-OES determined composition of *x*Nd: $BaTiO_3$ nanocrystals.

characters of perovskite $BaTiO_3$. While the small peak at 1061 cm^{-1} denotes the presence of $BaCO_3$ and the intensity decreases with the doping concentration. It is well-known that all phonons of cubic $Pm\bar{3}m$ symmetry are inactive to Raman modes, due to the isotropic distribution of electrostatic forces. The tetragonal P4*mm* space group exhibit eight Raman active modes described by $3[A_1(TO) + A_1(LO)] + 4[E(TO) + E(LO)] + B_1$. Among these, peaks at 184, 254, 518 cm^{-1} are assigned to the fundamental TO mode of A_1 symmetry, which generally exist both in cubic and tetragonal $BaTiO_3$[29]. The presence of bands at 184 cm^{-1} indicates a decoupling between the $A_1(TO)$ phonons, which can be induced by internal stress or lattice defects; whereas the asymmetry in the bands at 518 cm^{-1} suggests the existence of coupling of the TO modes associated with the tetragonal phase. The sharp peak at 307 cm^{-1} corresponding to $[B_1, E(TO + LO)]$ modes is attributed to the non-centrosymmetric regions arising from the displacement of titanium atoms from TiO_6 octahedra[30,31], suggesting the intrinsic structural distortion in the tetragonal $BaTiO_3$. The appearance of peak at 713 cm^{-1} is considered to the highest frequency longitudinal optical mode (LO). Besides, the higher relative intensity of the band *versus* other tetragonal bands for nanoparticles can be related to Ba vacancies in the $BaTiO_3$[32]. Herein, the relative intensity of the peaks at 307 and 518 cm^{-1} has been calculated to evaluate the tetragonality of as-synthetized *x*Nd: $BaTiO_3$ nanoparticles (the inset of Fig. 1f), which indicates a reduction trend of tetragonal distortions with the introduction of Nd ions.

Defect chemistry of *x*Nd: $BaTiO_3$ nanocrystals. It is well-known that the properties of $BaTiO_3$ are intimately related to the oxidation state of constituents. As-prepared *x*Nd: $BaTiO_3$ nanoparticles were characterized by X-ray photoelectron spectroscopy (XPS) to determine the binding state and chemical environment of elements. Figure 2a shows photoemission spectra of Ba *3d*, Ti *2p*, and O *1 s* in *x*Nd: $BaTiO_3$ nanoparticles. Peak deconvolution has been obtained by fitting the curves through the Gauss-Lorentz function. Peaks at 778 eV and 793.3 eV, respectively corresponding to the Ba $3d_{5/2}$ and Ba $3d_{3/2}$, are assigned to the perovskite structure of $BaTiO_3$. It is worth pointing out that the higher shoulders at 779.4 eV and 794.6 eV are usually associated with Ba vacancy point defects[33]. Note that the peak intensity at both 779.4 eV and 794.6 eV increases with the increase in Nd concentration, suggesting that Ba vacancy would boost with the introduction of Nd ions. In order to reach charge balance, the substitution of Nd^{3+} for Ba^{2+} would either convert Ti^{4+} to Ti^{3+} or generate Ti vacancies [16,34,35]. As reported in the literature[36,37], the existence of Ti^{3+} ions would lead to the broad of the Ti *2p* peak and a lower binding energy shoulder belonging to $2p_{3/2}$ peak at ~456 eV. While such a feature has not been detected in our samples (see Fig. 2a), thus excluding the existence of Ti^{3+}. Besides, the energy shift of Ti ions will extend over more than 4 eV in case of different coordination numbers[38]. Therefore, it can be concluded that the TiO_6 octahedron is preserved. Figure 2a also presents the XPS spectra of O *1 s* valence state, which shows one main peak corresponding to oxygen in $BaTiO_3$ (528.8 eV) and a broad peak caused by chemisorbed species and/or oxygen vacancies (531.9 eV)[39]. Previously, Lewis Wasson *et al.*[40] stated that the residual $BaCO_3$ could hardly be detected by XPS, as the carbonate took the form of discrete particles rather than the continuous surface layer. Combining our previous FT-IR results[27], it can be thus speculated that there exist chemisorbed OH^- ions.

Electron paramagnetic resonance (EPR) is a powerful technique to detect the presence of Ba and/or Ti vacancies[41]. Shown in Fig. 2b are the room-temperature EPR spectra of the pure $BaTiO_3$ and 1%Nd: $BaTiO_3$ nanopacrystals. Note that paramagnetic centers locate at g ~1.976 for both samples, implying the existence of Ba vacancies[42]. According to the previous report[43], the formation of Ti vacancies would present a paramagnetic center at $g = 2.004$~2.005. Nevertheless, this signature of Ti vacancies has not been observed in our samples. From the XPS and EPR results, it can be concluded that the charge compensation mechanism primarily involves the formation of Ba vacancies induced by Nd substitution into A-site.

In general, any imperfection (vacancies, lattice defects, impurities/doping, and local bond distortion[44]) can yield density of states within the band gap of an insulator. Figure 2c shows the UV-vis absorption spectra of *x*Nd: $BaTiO_3$ nanoparticles, with well-defined peaks and exponential tails. The Nd content dependent band gap (E_g) is plotted as the inset, from which we can see the band gap (E_g) initially decreases, then increases after $x > 1\%$ and eventually keeps constant at $x > 1.5$ mol%. This trend goes along with the Nd concentration dependent structural distortion observed in Raman spectra, where the structure of *x*Nd: $BaTiO_3$ turns toward pseudo-cubic structure with the incorporation of Nd (see the inset of Fig. 1f). Probably, it is the structural transition that results in the constant band gap for $x > 1.5$ mol%.

To further characterize structural imperfection, we measured the photoluminescence (PL) emission spectroscopy at room temperature excited by laser with the wavelength of 355 nm. In general, the PL emission occurs when there is polarization within the structure and some localized states in the band gap, *e.g.* free exciton levels, self-trapped excitons and defects or impurity levels[45]. Figure 2d displays the emission spectra of as-prepared *x*Nd: $BaTiO_3$ samples, where two peaks are observed at 446 nm and 554 nm, respectively. The former is considered to originate from a direct band excitation, intimately related to the distortion of TiO_6[46], as shown in blue dashed curves (blue wavelength region). The other peak is much broader (dashed green curves), which belongs to the

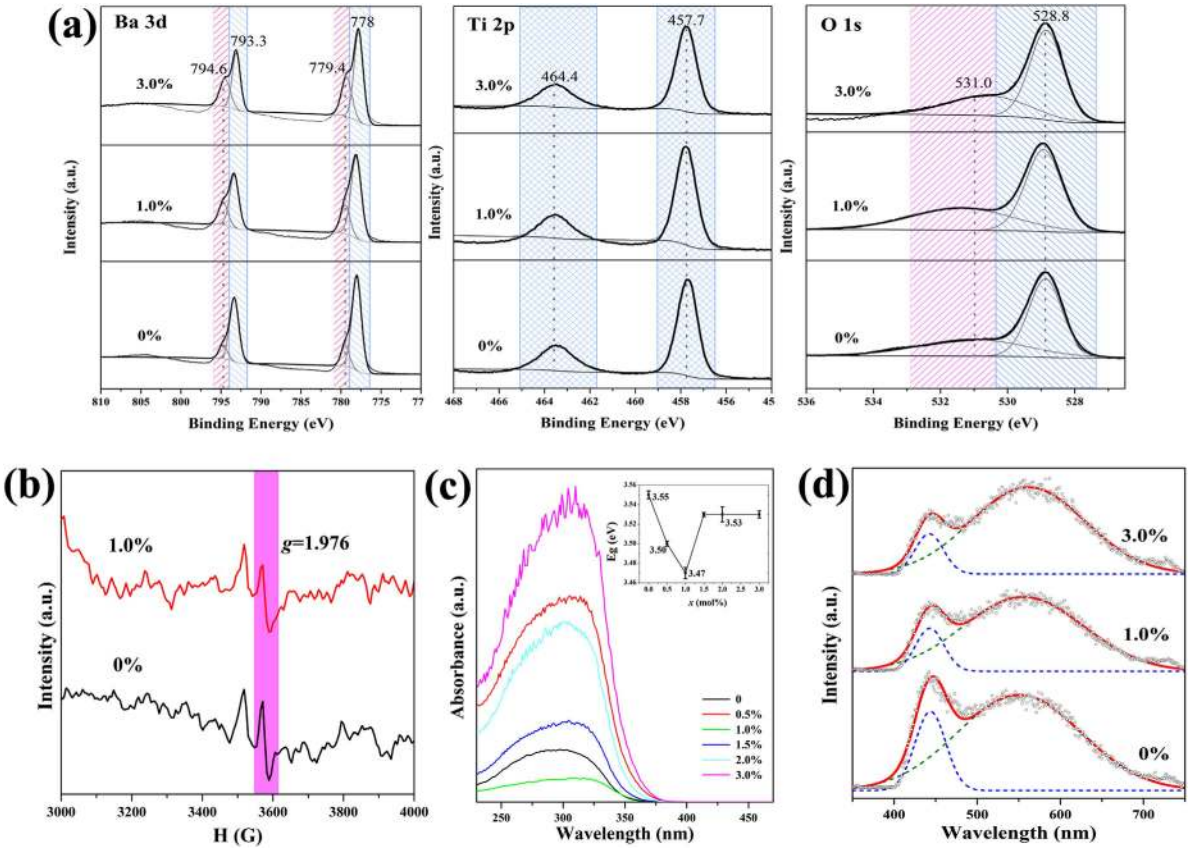

Figure 2. (**a**) XPS spectra for Ba *3d*, Ti *2p* and O *1 s* of *x*Nd: $BaTiO_3$ samples ($x = 0$, 1.0 and 3.0%): the black solid lines are the experimental data and the grey lines are the simulated curves; (**b**) Room-temperature EPR spectra of *x*Nd: $BaTiO_3$ ($x = 0$, 1%); (**c**) UV-vis spectra in the absorbance mode for indicated *x*Nd: $BaTiO_3$ samples; (**d**) Photoluminescence spectra of *x*Nd: $BaTiO_3$ powders, where circles (grey) are the experimental data, the solid lines represent simulated spectra, and dashed lines are simulated individual emission peaks.

yellow wavelength region according to Gaussian fit. This can be attributed to defects state within the band gap of the material[47]. The oxygen vacancies are considered as highly localized sensitive centers to trap electron from valance band and then the interaction of electron trapped with holes form self-trapped excitations. The radioactive recombination of the self-trapped excitations thus contributes to the emission of the yellow region. Compared to the low wavelength emission, this emission intensity increased gradually, indicating the oxygen vacancies defects increase with the incorporation of Nd ions.

Based on the above analysis, it can be concluded that when Nd is introduced into $BaTiO_3$, Ba vacancies as well as oxygen vacancies would simultaneously form to compensate the charge balance, which can be described as Equation (1):

$$2Nd + 2Ba_{Ba} + 2Ti_{Ti} + 6O_O \rightarrow 2Nd^{\bullet}_{Ba} + 2V''_{Ba} + V^{\bullet\bullet}_{O} + 2BaTiO_3 \quad (1)$$

Previously, such an occupation mechanism has been taken into consideration in the study of RE-doped $BaTiO_3$ ceramics. However, the existence of the Ba-vacancy induced by donor-doping mechanism(s) has never been demonstrated experimentally due to the mixtures of $Ba_{1-y}La_yTi_{1-y/4}O_3$ and other Ti-rich phase(s) such as $Ba_6Ti_{17}O_{40}$[48]. In our work, the formation of Ba-vacancy can be facilitated benefiting from the hydrothermal condition, where barium deficiencies are easily generated due to the introduction of protons[49].

Dielectric properties of *x*Nd: $BaTiO_3$ ceramics. It is well-known that the partial substitution of Ba^{2+} by RE^{3+} would result in the decrease of Curie temperature T_C (corresponding to a cubic-to-tetragonal structure transition). In our work, the tetragonal structure observed at room temperature (Fig. 1d–f) indicates that the Curie temperatures T_C of *x*Nd: $BaTiO_3$ nanocrystals still remain above room temperature, *i.e.* $T_C > 300$ K. In order to measure dielectric properties of our samples, *x*Nd: $BaTiO_3$ ceramics were fabricated from as-synthesized *x*Nd: $BaTiO_3$ nanocrystals by conventional pressureless sintering method at 1300 °C in air for 2 h.

As demonstrated in Fig. 3a, XRD patterns of *x*Nd: $BaTiO_3$ ceramics corresponds to the tetragonal structure with lattice parameters $a = b = 0.3994$ nm and $c = 0.4038$ nm (JCPDS: No.05-0626). The peak splitting of (002)/(200) observed at $2\theta \sim 46°$ for the samples with $x \leq 1$ mol% suggests their tetragonal structures. At higher Nd contents ($x > 1$ mol%), the peak splitting at around $2\theta \sim 46°$ cannot be recognized apparently. The results reveal that the introduction of Nd ions gives rise to the decrease in tetragonality, and induces the transition to pseudo-cubic

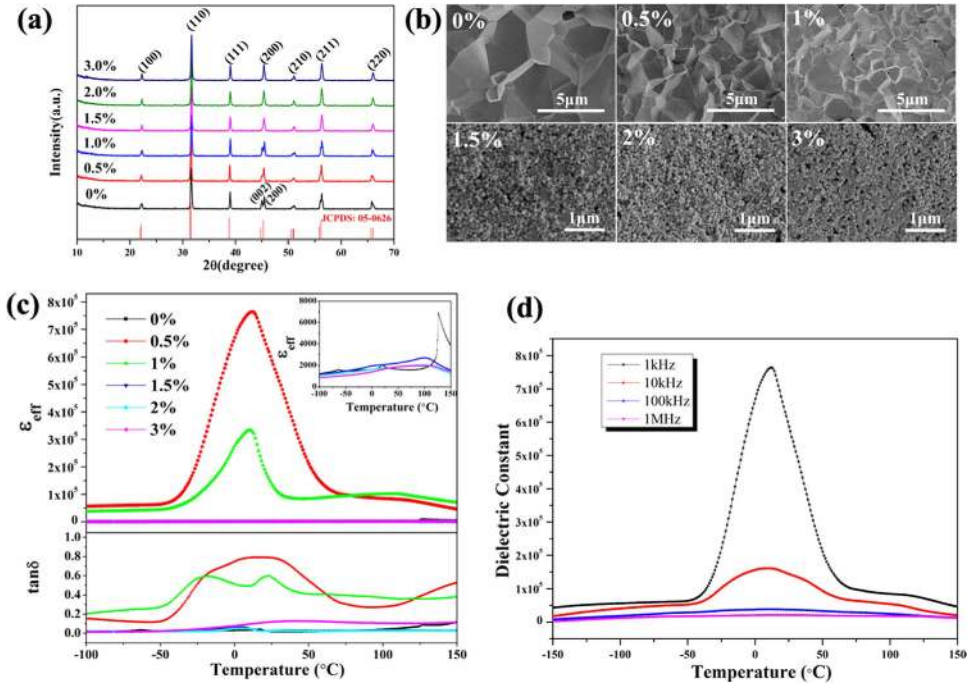

Figure 3. Properties of the Nd: $BaTiO_3$ ceramics sintered at 1300 °C for 2 h. (**a**) XRD pattern of the *x*Nd: $BaTiO_3$ samples; (**b**) SEM images of the *x*Nd: $BaTiO_3$ ceramics; (**c**) Temperature dependence of the permittivity and dielectric loss for the *x*Nd: $BaTiO_3$ ceramic samples measured at 1 kHz; (**d**) Permittivity versus temperature curves of 0.5%Nd: $BaTiO_3$ ceramics at different frequencies.

structure. Cross-sectional FE-SEM images shown in Fig. 3b indicate that ceramic grain size decreases with the Nd content increasing. It's observed that *x*Nd: $BaTiO_3$ ceramics with $x \leq 1$ mol% display compact microstructure, and their grain size is in the range of 1~5 μm. While the grain size of ceramic samples with $x > 1\%$ is comparable to its counterpart nanocrystals, and loosen microstructures are observed in these ceramics.

Figure 3c shows the temperature dependent relative dielectric constant ε_{eff} and tangent loss tanδ. Two features are remarkable: (1) the pure $BaTiO_3$ ceramics show a similar temperature dependence as conventional bulk ceramics with T_C ~125 °C, while the magnitude of ε_{eff} is about twofold higher; (2) the Nd introduction nonmonotonically enhances ε_{eff} and the colossal ε_{eff} ~7.6×10^5 is observed in 0.5%Nd: $BaTiO_3$ ceramics with tanδ ~0.8 at 12.2 °C.

In BT and rare-earth doped BT system, several explications have been proposed to explain the colossal dielectric constant, including internal barrier layer capacitance effect[50], hopping polarization[19], and electrode effect[51]. However, these ceramics either sintered in the non-oxidation atmosphere or sintered at a fast sintering rate with ultrafine grain size, which could result in the inner grain conductivity or the reduction of the Ti^{4+}. Moreover, giant permittivity values were reported in hexagonal barium titanate (*h*-$BaTiO_3$) single crystals[52], and the high permittivity values ~100,000 of the oxygen deficient materials were explained by the presence of interfacial boundaries consisting of crystal defects. In addition, it is reported that in $NaNbO_3$-doped $BaTiO_3$ system[53], colossal permittivity can be attributed to the high-energy electric state of Ba^+ (or $Ba^{2+} - e$) by Ba^{2+} obtaining an electron, which can create electron hopping conduction and increase conductivity of the ceramics. These charged defects like Ba^+ or Ba-vacancy are regarded to be responsible for the colossal permittivity[53,54]. However, neither the reduction of Ti^{4+} ions nor Ba^{2+} was observed in our work. In our viewpoint, the enhanced permittivity of *x*Nd: $BaTiO_3$ ceramics ($x \leq 1$ mol%) should be on the one hand attributed to the compact microstructure, resulting from the highly-active *x*Nd: $BaTiO_3$ nanoparticles. As we see in Fig. 3c, the permittivity of pure $BaTiO_3$ ceramics is about twofold higher than that of conventional bulk ceramics. In combination with defect chemistry discussed above, the enhancement of the permittivity can be on the other hand ascribed to the space-charge polarization[55], where the defects (*i.e.* Ba vacancies and O vacancies) induced by the dopants can act as additional dipoles. Since such a polarization cannot follow the alternating field at high frequency, the dielectric constant shows apparent decrease with the frequency arising. That is why the permittivity of the 0.5%Nd: $BaTiO_3$ sample decreases dramatically with increasing frequency, where the maximum dielectric constant of ~160,000 and ~30,000 is observed at 10 kHz and higher frequencies (≥100 kHz), respectively (Fig. 3d).

In all, previous reports[19,56] about the colossal permittivity in RE-doped $BaTiO_3$ ceramics were almost achieved with the assistant of special atmosphere and/or sintering techniques. This work demonstrate that conventional pressureless sintering condition in air is adequate to obtain *x*Nd: $BaTiO_3$ ceramics with colossal permittivity, as long as ceramic powders is of high sintering activity, which is a huge technique advantage in potential industrial production.

Conclusion

A series of *x*Nd: $BaTiO_3$ nanoparticles ($x = 0$ ~3.0 mol%) were successfully synthesized by a modified sol-hydrothermal method. It's demonstrated that all samples exhibit tetragonal phase and their tetragonality gradually decreases with the increasing Nd content. Shoulder peaks at high binding energy reveal the possible coexistence of Ba and O vacancies, while the probable emergence of reductive Ti^{3+} is excluded. Furthermore, the existence of Ba and O vacancies is confirmed by EPR and PL analysis, respectively. It's thereby proposed that the introduction of Nd ions into $BaTiO_3$ nanocrystals induce the simultaneously formation of Ba and O vacancies due to the valence equilibrium. Controlled by the RE content, dielectric constant of ceramic samples initially increases and then falls. Among them, 0.5%Nd: $BaTiO_3$ ceramics sintered from the nanopowders possess a room-temperature colossal permittivity (~760,000). The present work serves as a precedent and fundamental understanding of the crystal structure associated chemical defects of the RE-doped $BaTiO_3$ nanopowders, and deliberate efforts are on-going to better understand the underlying mechanism for the room-temperature colossal permittivity.

Methods

Synthesis of *x*Nd: $BaTiO_3$ nanoparticles. Nd-doped $BaTiO_3$ nanocrystals (*x*Nd: $BaTiO_3$, $x = 0$, 0.5, 1.0, 1.5, 2.0 and 3.0 mol%) were synthesized *via* a modified sol-hydrothermal method. To prepare TiO_2 sol, $Ti(OC_4H_9)_4$ and ethanol were fully blended with continuous stirring, and then a solution containing ethanol, HNO_3 and deionized water was slowly added. The as-prepared TiO_2 sol (10 ml) was then added to the solution of $Ba(Ac)_2$ in 40 ml deionized water. Simultaneously, appropriate amount of $Nd(NO_3)_3$ solution was added to control the doping concentration. During the process, the alkalinity (2 mol/L) was regulated by a KOH solution. The resulting mixture was stirred for 20 min, and then the Teflon vessel was put into a stainless-steel autoclave. The sealed autoclave was heated to 200 °C for 16 h, and then cooled to room temperature naturally. After the synthesis, the precipitates were washed with deionized water and ethanol in sequence several times. The resulting precipitates were collected and frozen in a refrigerator, and then dried by a freeze drying devices (Alpha 1-2LD, Christ, Germany).

Preparation of *x*Nd: $BaTiO_3$ Ceramics. The as-prepared *x*Nd: $BaTiO_3$ powders were mixed with 3 wt% PVA, pulverized using a mortar and pestle, and then pressed into pellets of 15 mm diameter under a uniaxial pressure of 8 MPa. After de-binding at 650 °C for 5 h, the green pellets were sintered at 1300 °C for 2 h in air by the conventional solid sintering method with a heating rate of 100 °C/h. Finally, the sintered ceramics were polished and coated with silver electrodes for electrical measurements.

Characterization. Powder X-ray diffraction (XRD) was collected on a Bruker D8 Advance diffractometer operating at 40 kV and 40 mA using Cu Kα radiation ($\lambda = 1.54178$ Å) to determine the structure of obtained samples. Raman spectra were recorded in the wavenumber range of 100~1100 cm^{-1} using a Jobin Yvon T64000 (Jobin Yvon, France) excited by the laser with a wavelength of 800 nm. The elemental composition was obtained by inductively coupled plasma-optical spectroscopy (ICP-OES) on the Optima 5300DV (PE, USA). The morphology and microstructure were obtained using a Hitachi S-4800 (Hitachi, Japan) field emission scanning electron microscope (FE-SEM). High-resolution transmission electron microscopy (HR-TEM) and selected area electron diffraction (SAED) images were obtained with the use of Tecnai G2 F30 S-TWIN (FEI, USA) microscope operated at 200 kV. The valence states of elements were analyzed by X-ray photoelectron spectroscopy (XPS) using an Escalab 250Xi (ThermoFisher Scientific, USA). Electron paramagnetic resonance (EPR) measurements were performed at room temperature using a Bruker A300-10/12 spectrometer operating at 9.85 GHz. Photoluminescence (PL) spectra were recorded at room temperature by exciting the samples through a 355 nm He–Cd laser on a QM40-NIR (PTI, USA). UV-vis diffuse reflectance spectra were recorded on a UV-visible spectrophotometer TU-1901 (PGeneral Instrument Inc., China) at room temperature with $BaSO_4$ as the reference and then converted into absorption spectra *via* Kubelka–Munk transformation. The dielectric properties of the samples were determined using the HP 4294 A (Hewlett-Packard, USA) impedance analyzer connected with a dc powder supply.

References

1. Xia, F. *et al.* Microwave absorption enhancement and electron microscopy characterization of $BaTiO_3$ nano-torus. *Nanoscale* **3,** 3860–3867 (2011).
2. Xia, X. *et al.* Solution synthesis of metal oxides for electrochemical energy storage applications. *Nanoscale* **6,** 5008–5048 (2014).
3. Raengthon, N., DeRose, V. J., Brennecka, G. L. & Cann, D. P. Defect mechanisms in high resistivity $BaTiO_3$–$Bi(Zn_{1/2}Ti_{1/2})O_3$ ceramics. *Appl. Phys. Lett.* **101,** 112904 (2012).
4. Song, Y. *et al.* Origin of colossal dielectric permittivity of rutile $Ti_{0.9}In_{0.05}Nb_{0.05}O_2$: single crystal and polycrystalline. *Sci. Rep*. **6,** 21478 (2016).
5. Hu, W. *et al.* Electron-pinned defect-dipoles for high-performance colossal permittivity materials. *Nat Mater.* **12,** 821–826 (2013).
6. Dean, J. S., Foeller, P. Y., Reaney, I. M. & Sinclair, D. C. A resource efficient design strategy to optimise the temperature coefficient of capacitance of $BaTiO_3$-based ceramics using finite element modelling. *J. Mater. Chem. A* **4,** 6896–6901 (2016).
7. Qiao, Y. *et al.* Thiophene polymer-grafted barium titanate nanoparticles toward nanodielectric composites. *Chem. Mater.* **26,** 5319–5326 (2014).
8. Maria, T. B., Massimo, V., Zhao, Z., Vincenzo, B. & Nanni, P. Synthesis of $BaTiO_3$ core-shell particles and fabrication of dielectric ceramics with local graded structure. *Chem. Mater.* **18,** 4002–4010 (2006).
9. Shi, T., Xie, L., Gu, L. & Zhu, J. Why Sn doping significantly enhances the dielectric properties of $Ba(Ti_{1-x}Sn_x)O_3$. *Sci. Rep*. **5,** 8606 (2015).
10. Tan, Y. *et al.* Unfolding grain size effects in barium titanate ferroelectric ceramics. *Sci. Rep*. **5,** 9953 (2015).
11. Krohns, S. *et al.* The route to resource-efficient novel materials. *Nat. Mater.* **10,** 899–901 (2011).
12. Ganguly, M. *et al.* Characterization and rietveld refinement of A-site deficient lanthanum doped barium titanate. *J. Alloy. Compd*. **579,** 473–484 (2013).
13. Li, Y., Yao, X. & Zhang, L. High permittivity neodymium-doped barium titanate sintered in pure nitrogen. *Ceram. Int.* **30,** 1325–1328 (2004).

14. Ben, L. & Sinclair, D. C. Anomalous Curie temperature behavior of A-site Gd-doped $BaTiO_3$ ceramics: The influence of strain. *App. Phys. Lett.* **98,** 092907 (2011).
15. Dawson, J. A., Sinclair, D. C., Harding, J. H. & Freeman, C. L. A-site strain and displacement in $Ba_{1-x}Ca_xTiO_3$ and $Ba_{1-x}Sr_xTiO_3$ and the consequences for the Curie temperature. *Chem. Mater.* **26,** 6104–6112 (2014).
16. Rabuffetti, F. A., Culver, S. P., Lee, J. S. & Brutchey, R. L. Local structural investigation of Eu^{3+}—doped $BaTiO_3$ nanocrystals. *Nanoscale* **6,** 2909–2914 (2014).
17. Ferrarelli, M. C., Tan, C. C. & Sinclair, D. C. Ferroelectric, electrical, and structural properties of Dy and Sc co-doped $BaTiO_3$. *J. Mater. Chem.* **21,** 6292 (2011).
18. Freeman, C. L., Dawson, J. A., Harding, J. H., Ben, L.-B. & Sinclair, D. C. The influence of A-site rare earth ion size in controlling the Curie temperature of $Ba_{1-x}RE_xTi_{1-x/4}O_3$. *Adv. Funct. Mater.* **23,** 491–495 (2013).
19. Guillemet-Fritsch, S. *et al.* Colossal permittivity in ultrafine grain size $BaTiO_{3-x}$ and $Ba_{0.95}La_{0.05}TiO_{3-x}$ materials. *Adv. Mater.* **20,** 551–555 (2008).
20. Shaikh, A. S. & Vest, R. W. Defect structure and dielectric properties of Nd_2O_3-modified $BaTiO_3$. *J. Am. Ceram. Soc.* **69,** 689–694 (1986).
21. Hirose, N., Skakle, J. M. S. & West, A. R. Doping mechanism and permittivity correlations in Nd-doped $BaTiO_3$. *J. Electroceram.* **3,** 233–238 (1999).
22. Yao, Z. *et al.* Structure and dielectric behavior of Nd-doped $BaTiO_3$ perovskites. *Mater. Chem. Phys.* **109,** 475–481 (2008).
23. Wei, X. *et al.* Size-controlled synthesis of $BaTiO_3$ nanocrystals via a hydrothermal route. *Mater. Lett.* **62,** 3666–3669 (2008).
24. Lin, L., Sun, X., Jiang, Y. & He, Y. Sol-hydrothermal synthesis and optical properties of Eu^{3+}, Tb^{3+}—codoped one-dimensional strontium germanate full color nano-phosphors. *Nanoscale* **5,** 12518–12531 (2013).
25. Zhang, W., Cao, L., Su, G. & Liu, W. Influence of microstructure on dielectric properties of Nd-doped barium titanate synthesized by hydrothermal method. *J. Mater. Sci.: Mater. Electron.* **24,** 1801–1806 (2013).
26. Zhang, W. *et al.* Effects of neodymium doping on dielectric and optical properties of $Ba_{1-x}Nd_xTi_{1.005}O_3$ ceramics. *Ceram.-Silikáty* **57,** 146–150 (2013).
27. Zheng, H., Zhu, K., Wu, Q., Liu, J. & Qiu, J. Preparation and characterization of monodispersed $BaTiO_3$ nanocrystals by sol-hydrothemal method. *J. Cryst. Growth* **363,** 300–307 (2013).
28. Su, R. *et al.* Silver-modified nanosized ferroelectrics as a novel photocatalyst. *Small* **11,** 202–207 (2015).
29. Busca, G., Buscaglia, V., Leoni, M. & Nanni, P. Solid-state and surface spectroscopic characterization of $BaTiO_3$ fine powders. *Chem. Mater.* **6,** 955–961 (1994).
30. Rabuffetti, F. A. & Brutchey, R. L. Structural evolution of $BaTiO_3$ nanocrystals synthesized at room temperature. *J. Am. Chem. Soc.* **134,** 9475–9487 (2012).
31. Smith, M. B. *et al.* Crystal structure and the paraelectric-to-ferroelectric phase transition of nanoscale $BaTiO_3$. *J. Am. Chem. Soc.* **130,** 6955–6963 (2008).
32. Lin, M. F., Thakur, V. K., Tan, E. J. & Lee, P. S. Dopant induced hollow $BaTiO_3$ nanostructures for application in high performance capacitors. *J. Mater. Chem.* **21,** 16500 (2011).
33. Woong Lee, K., Siva Kumar, K., Heo, G., Seong, M. J. & Yoon, J. W. Characterization of hollow $BaTiO_3$ nanofibers and intense visible photoluminescence. *J. Appl. Phys.* **114,** 134303 (2013).
34. Freeman, C. L. *et al.* Energetics of donor-doping, metal vacancies, and oxygen-loss in A-site rare-earth-doped $BaTiO_3$. *Adv. Funct. Mater.* **23,** 3925–3928 (2013).
35. Freeman, C. L. *et al.* A new potential model for barium titanate and its implications for rare-earth doping. *J. Mater. Chem.* **21,** 4861 (2011).
36. Jena, H. *et al.* X-ray photoelectron spectroscopic investigations on cubic $BaTiO_3$, $BaTi_{0.9}Fe_{0.1}O_3$ and $Ba_{0.9}Nd_{0.1}TiO_3$ systems. *Appl. Surf. Sci.* **254,** 7074–7079 (2008).
37. Liu, X. *et al.* Green synthetic approach for Ti^{3+} self-doped TiO_{2-x} nanoparticles with efficient visible light photocatalytic activity. *Nanoscale* **5,** 1870–1875 (2013).
38. Ehre, D., Cohen, H., Lyahovitskaya, V. & Lubomirsky, I. X-ray photoelectron spectroscopy of amorphous and quasiamorphous phases of $BaTiO_3$ and $SrTiO_3$. *Phys. Rev. B* **77,** 184106 (2008).
39. Souza, A. E. *et al.* Photoluminescence activity of $Ba_{1-x}Ca_xTiO_3$: dependence on particle size and morphology. *J. Mater. Chem. C* **2,** 7056 (2014).
40. Wegmann, M., Watson, L. & Hendry, A. XPS analysis of submicrometer barium titanate powder. *J. Am. Ceram. Soc.* **87,** 371–377 (2008).
41. Lu, D. Y. & Cui, S. Z. Defects characterization of Dy-doped $BaTiO_3$ ceramics via electron paramagnetic resonance. *J. Eur. Ceram. Soc.* **34,** 2217–2227 (2014).
42. Dunbar, T. D., Warren, W. L., Tuttle, B. A., Randall, C. A. & Tsur, Y. Electron paramagnetic resonance investigations of lanthanide-doped barium titanate. *J. Phys. Chem. B* **108,** 908–917 (2003).
43. Priebe, J. B. *et al.* Water reduction with visible light: synergy between optical transitions and electron transfer in Au-TiO_2 catalysts visualized by *in situ* EPR spectroscopy. *Angew. Chem.* **52,** 11420–11424 (2013).
44. Longo, V. M. *et al.* Structural conditions that leads to photoluminescence emission in $SrTiO_3$: An experimental and theoretical approach. *J. Appl. Phys.* **104,** 023515 (2008).
45. Yu, J., Sun, J., Chu, J. & Tang, D. Light-emission properties in nanocrystalline $BaTiO_3$. *Appl. Phys. Lett.* **77,** 2807 (2000).
46. Jiang, S. *et al.* Growth and bending-sensitive photoluminescence of a flexible $PbTiO_3$/ZnO nanocomposite. *ACS Appl. Mater. Inter.* **6,** 10935–10940 (2014).
47. Fuentes, S., Barraza, N., Veloso, E., Villarroel, R. & Llanos, J. Effects of Eu substitution on luminescent and magnetic properties of $BaTiO_3$ nanomaterials. *J. Alloy. Compd.* **569,** 52–57 (2013).
48. Morrison, F. D., Sinclair, D. C. & West, A. R. Electrical and structural characteristics of lanthanum-doped barium titanate ceramics. *J. Appl. Phys.* **86,** 6355–6366 (1999).
49. Hennings, D., Metzmacher, C. & Schreinemacher, B. Defect chemistry and microstructure of hydrothermal barium titanate. *J. Am. Ceram. Soc.* **84,** 179–82 (2001).
50. Chung, U. C., Elissalde, C., Mornet, S., Maglione, M. & Estournès, C. Controlling internal barrier in low loss $BaTiO_3$ supercapacitors. *Appl. Phys. Lett.* **94,** 072903 (2009).
51. Han, H. *et al.* Origin of colossal permittivity in $BaTiO_3$ via broadband dielectric spectroscopy. *J. Appl. Phys.* **113,** 024102 (2013).
52. Sinclair, C. *et al.* Structure and electrical properties of oxygen-deficient hexagonal $BaTiO_3$. *J. Mater. Chem.* **9,** 1327–1331 (1999).
53. Cao, W., Xu, L., Ismail M. & Huang, L. Colossal dielectric constant of $NaNbO_3$ doped $BaTiO_3$ ceramics. *Mater. Sci.-Poland* **34,** 322–329 (2016).
54. Iguchi, F. *et al.* The relationship between chemical composition distributions and specific grain boundary conductivity in Y-doped $BaZrO_3$ proton conductors. *Solid State Ionics* **180,** 563–568 (2009).
55. Kim, S. S., Kim, S. T., Yoon, Y. C. & Lee, K. S. Magnetic, dielectric, and microwave absorbing properties of iron particles dispersed in rubber matrix in gigahertz frequencies. *J. Appl. Phys.* **97,** 10F905 (2005).
56. Valdez-Nava, Z. *et al.* Colossal dielectric permittivity of $BaTiO_3$-based nanocrystalline ceramics sintered by spark plasma sintering. *J. Electroceram.* **22,** 238–244 (2008).

Acknowledgements

This work was supported by the National Natural Science Foundation of China (NSFC No. 51372114 and 51672130), the Research Fund of State Key Laboratory of Mechanics and Control of Mechanical Structures (Nanjing University of Aeronautics and Astronautics) (Grant No. 0514Y01), A Project Funded by the Priority Academic Program Development of Jiangsu Higher Education Institutions (PAPD).

Author Contributions

Qiaomei Sun and Kongjun Zhu conceived the experimental research; Qiaomei Sun executed the experiments; Qilin Gu and Rongyin Jin devoted to the data analysis and manuscript modification; Jinsong Liu conducted XRD, UV-vis and FE-SEM measurements; Jing Wang performed XPS and Raman characterization; Jinhao Qiu contributed to the dielectric measurement; Qiaomei Sun and Qilin Gu wrote the manuscript with contribution from all authors; everyone participated in discussions and analysis of the results.

Additional Information

Supplementary information accompanies this paper at http://www.nature.com/srep

Competing financial interests: The authors declare no competing financial interests.

How to cite this article: Sun, Q. *et al.* Crystalline Structure, Defect Chemistry and Room Temperature Colossal Permittivity of Nd-doped Barium Titanate. *Sci. Rep.* **7**, 42274; doi: 10.1038/srep42274 (2017).

Publisher's note: Springer Nature remains neutral with regard to jurisdictional claims in published maps and institutional affiliations.